

# A Novel Pseudo-Spectral Time-Domain Theory of Magnetic Neutron Scattering Illustrated Using A Uniformly Magnetized Sphere

Kun Chen

<sup>a</sup>Key Laboratory of Quantum Optics, Department of Aerospace Laser Technology and Systems, Shanghai Institute of Optics and Fine Mechanics, Chinese Academy of Sciences, Shanghai, 201800, China

---

## Abstract

A universal numerical method is developed for the investigation of magnetic neutron scattering. By applying the pseudospectral-time-domain (PSTD) algorithm to the spinor version of the Schrödinger equation, the evolution of the spin-state of the scattered wave can be solved in full space and time. This extra spin degree of freedom brings some unique new features absent in the numerical theory on the scalar wave scatterings [1]. Different numerical stability condition has to be re-derived due to the coupling between the different spin components. As the simplest application, the neutron scattering by the magnetic field of a uniformly magnetized sphere is studied. The PSTD predictions are compared with those from the Born-approximation. This work not only provides a systematic tool for analyzing spin-matter interactions, but also builds the forward model for testing novel neutron imaging methodologies, such as the newly developed thermal neutron Fourier-transform ghost imaging.

*Keywords:* magnetic neutron scattering, Fresnel region, PSTD, total-field/scattered-field, ghost imaging

---

## 1. Introduction

Magnetic neutron scattering is the preferred method to probe materials' magnetic structure. As a neutral particle, neutron can penetrate deep into materials. The nuclear magnetic moment of neutron leads to its direct interaction with unpaired electrons of atoms. Instrumental developments of various experimental schemes have tremendously broadened the knowledge about vast magnetic phenomena and disclosed the underlining dynamics [2–6]. Especially, the polarized neutron scattering has provided detailed and unambiguous information about the magnetic structures.

Theoretical expressions for the spin-state cross-sections of magnetic neutron scattering *in the far field* have been derived from the Schrödinger equation using

---

*Email address:* kunchen@siom.ac.cn, kunchen@alum.mit.edu (Kun Chen)

the Fermi's golden rule [2]. However, these mathematical formulas of cross-sections mainly serve as a qualitative interpretation of the experimental results. The magnetic structure deduced from the data would be represented by form factors in the theory. Given a general magnetization distribution, it is hard to quantitatively predict the scattering cross-section. Furthermore, the existing theories only predict the far-field behavior. When it comes to the scattered waves in the near field and the mid field (i.e., the Fresnel region), the traditional methods would be incapable to provide reasonable results.

There is a separate motivation to calculate the magnetically scattered wave function in the Fresnel region (FR). Over the past two decades, there have been intense developments on a lensless imaging methodology, referred to as the ghost imaging (GI) [7–13]. GI explores the fourth-order correlation of the wave fields. In a typical GI setup, the spatially-incoherent incident beam, either a bosonic or a fermionic field, is split into a sample arm and a reference arm. Spatially resolved wavefront detection is employed in the reference arm only, while the signals in the sample arm are collected by a bucket detector. The bosonic GI is enlightened by the Hanbury Brown and Twiss (HBT) effect [14, 15], and exploits the photon bunching phenomenon arising from the bosonic statistics of optical fields [7, 8]. On the other hand, the fermionic GI, still at its early stage of development, utilizes the antibunching phenomenon of fermionic matter waves [12, 13], dictated by the Pauli's exclusive principle and observed in a series of experiments [16–19]. The Fourier-transform (FT) implementation of both GIs can achieve microscopic imaging of the matter, potentially with de Broglie wavelength level resolution. Unlike the conventional imaging techniques which detect the far-field signals, the FT GIs selectively detect the signals from the FR. This is the crucial difference between this new and the existing, old imaging strategies.

In recent years, we established a microscopic imaging theory for atomic and magnetic structures based on thermal neutron FT GI. The theory intends to reconstruct the distribution of atom sites and material magnetizations from experimental data. This falls into the category of inverse problems. To test the validity and accuracy of this theory, a numerical simulation is necessary before the actual experiment can be attempted. In short, a forward model is needed to generate the "experimental" data. Neutron scattering by matter involves two independent processes, nuclear scattering by the nuclei of atom sites and magnetic scattering by the magnetic structure of the material. Both belong to the potential scattering problems of the Schrödinger equation. Because the range of nuclear forces is within 10 fm and the wavelengths of thermal neutrons are at the order of 1 Å to a few nm, the nuclear interaction can be easily handled as a delta potential scattering [2]. The actual difficulty lies in the latter one, in which there is no easy way to calculate the scattering by an arbitrary magnetic field. In addition, fermionic GI is a fully quantum exploitation in the FR. This fact rules out the Monte Carlo (MC) method. MC treats the incidence as a bunch of particles undergoing a series of collisions with a random matrix of scatterers. The quantum behavior is only reflected in the form of scattering phase function, i.e., the deflection of the particle's flying direction after each collision is sampled in an approximate quantum way. While between consecutive collisions, the particle goes through straight line free-flying, ignoring all wave nature and precluding any

quantum cross-talks between paths. In addition, the scatterings at different sites are treated as independent ones, without any interference. Therefore, preserving the quantum behavior requires a startup purely from the first principle, the Schrödinger equation. However, conventional scattering analyses focus on the far field and thus are inadequate for GI. All these considerations demand a completely new treatment of the magnetic scattering.

In the first step toward this final goal, we recently successfully built a numerical theory to universally solve the quantum potential scattering wave function in full 3D regions, ranging from the near field, to the FR, and to the far field [1]. Yet this theory still lacks the spin degree of freedom, and has to be extended to spinor wave functions before it can be applied to the magnetic studies. In this paper, we will finish the extra steps and present a forward model calculation on the neutron scattering by a magnetic field.

## 2. PSTD algorithm for solving the Schrödinger equation of spinor wave

The quantum scattering of the neutron wave by a magnetic field is governed by the Schrödinger equation [2],

$$i\hbar \frac{\partial \Psi}{\partial t} = -\frac{\hbar^2}{2m_n} \nabla^2 \Psi - \boldsymbol{\mu}_n \cdot \mathbf{B} \Psi. \quad (1)$$

Here,  $m_n$  is the neutron mass,  $\boldsymbol{\mu}_n = -\gamma\mu_N\boldsymbol{\sigma}$  the magnetic dipole moment of the neutron,  $\boldsymbol{\sigma}$  the Pauli spin operator for the neutron,  $\gamma = 1.913$  and  $\mu_N$  the nuclear magneton,  $\mathbf{B}$  the magnetic induction, and  $\Psi$  the spinor wave function. Apply the same dimensionless procedure [1], i.e., define

$$\tau = \omega_0 t, \quad (\bar{x}, \bar{y}, \bar{z}) = (k_0 x, k_0 y, k_0 z), \quad (2)$$

where  $\omega_0 = E_0/\hbar$  and  $k_0 = P_0/\hbar = \sqrt{2m_n E_0}/\hbar$ . For a monochromatic plane wave incidence,  $E_0$  and  $P_0$  would be the energy and momentum of the neutron wave, respectively. For a pulsed plane wave incidence,  $E_0$  and  $P_0$  would be the values at the central frequency. Using the dimensionless variables of Eq. (2), Eq. (1) is rescaled to

$$\frac{\partial \Psi}{\partial \tau} = i\bar{\nabla}^2 \Psi - i\frac{\gamma\mu_N}{E_0} \boldsymbol{\sigma} \cdot \mathbf{B} \Psi, \quad (3)$$

and  $\bar{\nabla} = \hat{x} \frac{\partial}{\partial \bar{x}} + \hat{y} \frac{\partial}{\partial \bar{y}} + \hat{z} \frac{\partial}{\partial \bar{z}}$ . In this way, the rescaled Schrödinger equation becomes one on pure numbers. This greatly simplifies the derivation of numerical algorithms.

There is no analytical solution to Eq. (3) for a general distribution of magnetic field  $\mathbf{B}$ . However, numerical solution can be sought for a localized  $\mathbf{B}$ , even of an arbitrary shape. Highly efficient parallel computing is inevitable. The Pauli spin operators in Eq. (3) are represented by  $2 \times 2$  matrices. Thus the spinor wave function  $\Psi$  takes the form of a  $2 \times 1$  matrix, containing two spin components. The layout of the numerical lattice model here is very similar to the scalar wave studies (Fig. 1) [1].

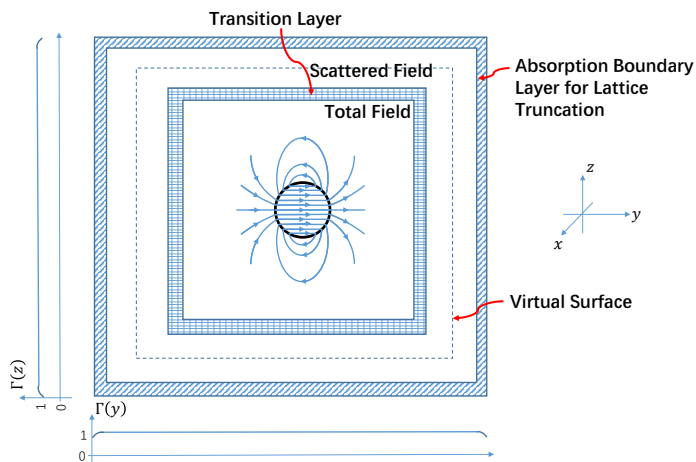


Figure 1: Setup of the Internal Model

Again, we employ the total-field/scattered-field (TF/SF) scheme and the PSTD approach to the partial derivatives. The terminology TF/SF stems from the computational electrodynamics [20]. The term "field" in the Schrödinger world refers to the probing particle's matter wave field. In Fig. 1, the computation domain is divided into shell-like regions. The outmost numerical absorption boundary serves to truncate the space lattice and converts the computation in infinite domain to finite domain. Three  $\Gamma$  functions, one along each coordinate dimension, are multiplied to the wave function at each iteration to impose the absorption boundary condition (ABC). The small smooth dips near the left and right ends of  $\Gamma(y)$  attenuate the wave function near the left and right boundaries. The boundaries in the  $x$  and  $z$  directions are controlled in the same way by  $\Gamma(x)$  and  $\Gamma(z)$ . The 3D ABC multiplier is the product  $\Gamma(\mathbf{r}) = \Gamma(x)\Gamma(y)\Gamma(z)$ , and the 1D- $\Gamma$  function is chosen to be [1, 21]

$$\Gamma(d) = \exp\left(-\frac{U_0}{\cosh^2(\alpha d)} \Delta\tau\right), \quad (4)$$

where  $d$  is the distance (the smaller one) from the left or right boundaries. The inner core in Fig. 1, referred to as the TF, encloses all the magnetic fields and contains all the neutron-target interactions; whereas the SF is the free-propagating region of the scattered waves. In the TF, the up/down spin components will inter-exchange due to the off-diagonal elements of  $\sigma_x$  and  $\sigma_y$ , whereas exterior to the TF, the up/down spin components decouple and the spin states are preserved. The transition layer connects the TF and the SF, incorporates the incident wave into the model, and smoothly converts the total wave function (in the TF) to the pure scattered wave function (in the SF), based on the fact that

$$\Psi^{\text{total}} = \Psi^{\text{scat}} + \Psi^{\text{inc}}, \quad (5)$$

where  $\Psi^{\text{total}}$ ,  $\Psi^{\text{scat}}$  and  $\Psi^{\text{inc}}$  are the total, scattered and incident wave functions, respectively. It is important to stress that, unlike the electromagnetic studies where the

TF could be tightened to the permittivity and permeability structure and stop at the material boundary, in the quantum case the magnetic field extends far beyond the underlying magnetization structure. Since the magnetic interaction is long-range, a reasonable cutoff on range is required to limit the size of TF. The field intensity of a magnetic dipole typically decays as  $r^{-3}$ , so in practice a TF should be at least one order of magnitude larger than the magnetization size.

Similar to the studies on the Maxwell's equations [22] and the Schrödinger equation of scalar-waves [1], we introduce a taper function  $\zeta(\bar{\mathbf{r}}) = \zeta_x(\bar{x})\zeta_y(\bar{y})\zeta_z(\bar{z})$  on the space lattice, such that  $\zeta(\bar{\mathbf{r}})$  is 0 for  $\bar{\mathbf{r}}$  in the SF and ABC, 1 for  $\bar{\mathbf{r}}$  in the TF, and smoothly rises from 0 to 1 for  $\bar{\mathbf{r}}$  across the transition layer. The optimal choice of the  $\zeta$  function is discussed in Ref. [1]. Consequently, a new wave function

$$\tilde{\Psi}(\bar{\mathbf{r}}, \tau) = \Psi^{\text{scat}}(\bar{\mathbf{r}}, \tau) + \zeta(\bar{\mathbf{r}})\Psi^{\text{inc}}(\bar{\mathbf{r}}, \tau) \quad (6)$$

would represent the total wave function in the TF and the pure scattered wave function in the SF. Recall that both the incident wave function  $\Psi^{\text{inc}}(\bar{\mathbf{r}}, \tau)$  and the scattered wave function  $\Psi^{\text{sca}}(\bar{\mathbf{r}}, \tau)$  satisfy the Schrödinger equation in free space. Combining with Eq. (3), we have

$$\frac{\partial \tilde{\Psi}(\bar{\mathbf{r}}, \tau)}{\partial \tau} = i\bar{\nabla}^2 \tilde{\Psi}(\bar{\mathbf{r}}, \tau) - i\frac{\gamma\mu N}{E_0} \boldsymbol{\sigma} \cdot \mathbf{B}(\bar{\mathbf{r}}) \tilde{\Psi}(\bar{\mathbf{r}}, \tau) - i[\bar{\nabla}^2 \zeta(\bar{\mathbf{r}}) + 2\bar{\nabla} \zeta(\bar{\mathbf{r}}) \cdot \bar{\nabla}] \Psi^{\text{inc}}(\bar{\mathbf{r}}, \tau). \quad (7)$$

Because  $\mathbf{B}(\bar{\mathbf{r}}) = 0$  for regions outside the TF, the scattering potential is well defined in the entire computation domain. As  $\tilde{\Psi}(\bar{\mathbf{r}}, \tau)$  in the SF is automatically the scattered wave function, the task of solving the original scattering problem in infinite space is reduced to solving Eq. (7) on the truncated lattice of Fig. 1.

Now we explicitly express the spinor  $\tilde{\Psi}$  in the matrix form

$$\tilde{\Psi} = \begin{pmatrix} \psi_u \\ \psi_d \end{pmatrix}. \quad (8)$$

Substituting the Pauli matrices into Eq. (7), we have the explicit equations,

$$\begin{aligned} \frac{\partial \psi_u}{\partial \tau} &= i\bar{\nabla}^2 \psi_u - i\frac{\gamma\mu N}{E_0} (B_z \psi_u + B_x \psi_d - iB_y \psi_d) \\ &\quad - i[\bar{\nabla}^2 \zeta \psi_u^{\text{inc}} + 2\bar{\nabla} \zeta \cdot \bar{\nabla} \psi_u^{\text{inc}}], \end{aligned} \quad (9)$$

$$\begin{aligned} \frac{\partial \psi_d}{\partial \tau} &= i\bar{\nabla}^2 \psi_d - i\frac{\gamma\mu N}{E_0} (B_x \psi_u + iB_y \psi_u - B_z \psi_d) \\ &\quad - i[\bar{\nabla}^2 \zeta \psi_d^{\text{inc}} + 2\bar{\nabla} \zeta \cdot \bar{\nabla} \psi_d^{\text{inc}}]. \end{aligned} \quad (10)$$

The three terms on the r.h.s. of Eqs. (9) and (10) correspond to the kinetic energy, the potential energy and the incident wave contribution, respectively. Apply the central finite difference to the time derivative on the l.h.s. and implement pseudospectral operation on the kinetic energy term, we obtain the iteration updating formulas

$$\psi_u \Big|_{i,j,k}^{n+1} = \Gamma_{i,j,k} \left\{ \psi_u \Big|_{i,j,k}^{n-1} + 2\Delta\tau \left[ K_u \Big|_{i,j,k}^n + P_u \Big|_{i,j,k}^n + I_u \Big|_{i,j,k}^n \right] \right\}, \quad (11)$$

$$\psi_d \Big|_{i,j,k}^{n+1} = \Gamma_{i,j,k} \left\{ \psi_d \Big|_{i,j,k}^{n-1} + 2\Delta\tau \left[ K_d \Big|_{i,j,k}^n + P_d \Big|_{i,j,k}^n + I_d \Big|_{i,j,k}^n \right] \right\} \quad (12)$$

for indices  $i, j, k$  over the entire lattice. Here  $\Gamma_{i,j,k}$  is the grid value of the mask function  $\mathbb{I}(\mathbf{r})$ , introduced as the ABC for the truncation of the lattice, equivalent to a complex absorption potential (CAP) [21, 23]. The increments due to the kinetic energy are

$$K_u \Big|_{i,j,k}^n = -i\eta \sum_{\ell=\bar{x},\bar{y},\bar{z}} \mathcal{F}_\ell^{-1} [k_\ell^2 \mathcal{F}_\ell [\psi_u]] \Big|_{i,j,k}^n, \quad (13)$$

$$K_d \Big|_{i,j,k}^n = -i\eta \sum_{\ell=\bar{x},\bar{y},\bar{z}} \mathcal{F}_\ell^{-1} [k_\ell^2 \mathcal{F}_\ell [\psi_d]] \Big|_{i,j,k}^n \quad (14)$$

for indices  $i, j, k$  over the entire lattice, and  $\eta = \text{sinc}(\Delta\tau)$  is a correction factor to cancel the numerical phase velocity error caused by the time discretization [1]. The increments due to the potential energy are

$$P_u \Big|_{i,j,k}^n = -i \frac{\gamma\mu_N}{E_0} \left[ B_z \Big|_{i,j,k} \psi_u \Big|_{i,j,k}^n + (B_x - iB_y) \Big|_{i,j,k} \psi_d \Big|_{i,j,k}^n \right], \quad (15)$$

$$P_d \Big|_{i,j,k}^n = -i \frac{\gamma\mu_N}{E_0} \left[ (B_x + iB_y) \Big|_{i,j,k} \psi_u \Big|_{i,j,k}^n - B_z \Big|_{i,j,k} \psi_d \Big|_{i,j,k}^n \right] \quad (16)$$

for indices  $i, j, k$  within the TF zone. The increments due to the injection of the incident wave are

$$I_u \Big|_{i,j,k}^n = -i \left[ \bar{\nabla}^2 \zeta \psi_u^{\text{inc}} + 2\bar{\nabla} \zeta \cdot \bar{\nabla} \psi_u^{\text{inc}} \right] \Big|_{i,j,k}^n, \quad (17)$$

$$I_d \Big|_{i,j,k}^n = -i \left[ \bar{\nabla}^2 \zeta \psi_d^{\text{inc}} + 2\bar{\nabla} \zeta \cdot \bar{\nabla} \psi_d^{\text{inc}} \right] \Big|_{i,j,k}^n \quad (18)$$

for indices  $i, j, k$  within the transition layer only. Note that the analytical expressions of  $\zeta$  and  $\bar{\nabla} \zeta$  are known. Under the incidence of a monochromatic plane wave or a plane wave of Gaussian-shaped pulse, the  $\psi^{\text{inc}}$  and  $\bar{\nabla} \psi^{\text{inc}}$  are also known analytically beforehand. Therefore,  $I_u$  and  $I_d$  can be prepared before the code run. On the other hand, for the plane wave incidence of a pulsed wavepacket of arbitrary time-profile, as the wavepacket will spread over time during the propagation, a separate, independent one-dimensional free-space Schrödinger equation (i.e., with the potential equal to 0) is often solved concurrently with Eqs. (9) and (10) to provide the  $\psi_u^{\text{inc}}, \psi_d^{\text{inc}}$  and their first derivatives during the time marching.

Because outside the TF the magnetic induction  $\mathbf{B} = 0$ , the spin status of the neutron wave is preserved. The up and down components of the scattered spinor wave act like two independent scalar waves. The procedure on the scattered scalar wave [1] can be directly applied. The virtual surface data for the up and down waves are stored separately, and the near-to-distant-field transformation can be performed independently for each spin.

### 3. Stability Condition

The iterations (Eqs. (11)-(12)) will diverge quickly if the time-marching step is large than a bound. However, the stability condition for the spinor wave function (Eq. (1)) cannot employ the conclusion for the scalar wave function [1]. The off-diagonal elements of  $\boldsymbol{\sigma} \cdot \mathbf{B}$  create coupling terms between the differential equations

of the up and down components. To proceed, again we adopt the approach of Ref. [24]. The discrete form of Eq. (1) is first separated into a temporal eigenvalue problem and a spatial eigenvalue problem, i.e.,

$$i\hbar \frac{\Psi^{n+1} - \Psi^{n-1}}{2\Delta t} = \lambda_t \Psi^n, \quad (19)$$

$$-\frac{\hbar^2}{2m} \nabla^2 \Psi(\mathbf{r}, t) + \gamma \mu_N \boldsymbol{\sigma} \cdot \mathbf{B}(\mathbf{r}) \Psi(\mathbf{r}, t) = \lambda_s \Psi(\mathbf{r}, t). \quad (20)$$

The matrix  $\boldsymbol{\sigma} \cdot \mathbf{B}(\mathbf{r})$  is Hermitian. Its eigenvalues are  $\pm B(\mathbf{r})$ , where

$$B(\mathbf{r}) = \sqrt{B_x^2(\mathbf{r}) + B_y^2(\mathbf{r}) + B_z^2(\mathbf{r})}. \quad (21)$$

Their corresponding eigenvectors (normalized) form the column vectors of a transform  $\mathcal{A}(\mathbf{r})$  such that

$$\mathcal{A}^\dagger(\mathbf{r})\mathcal{A}(\mathbf{r}) = \mathcal{A}(\mathbf{r})\mathcal{A}^\dagger(\mathbf{r}) = I, \quad \mathcal{A}^\dagger(\mathbf{r})\boldsymbol{\sigma} \cdot \mathbf{B}(\mathbf{r})\mathcal{A}(\mathbf{r}) = \begin{pmatrix} B(\mathbf{r}) & 0 \\ 0 & -B(\mathbf{r}) \end{pmatrix}. \quad (22)$$

Because the transform  $\mathcal{A}(\mathbf{r})$  is time irrelevant,\* Eq. (19) is equivalent to

$$i\hbar \frac{[\mathcal{A}^\dagger(\mathbf{r})\Psi]^{n+1} - [\mathcal{A}^\dagger(\mathbf{r})\Psi]^{n-1}}{2\Delta t} = \lambda_t [\mathcal{A}^\dagger(\mathbf{r})\Psi]^n, \quad (23)$$

i.e.,  $\mathcal{A}^\dagger(\mathbf{r})\Psi$  is a linear combination of the up and down components of the original  $\Psi$ . The derivation of the condition for  $\lambda_t$  is the same as the scalar wave function case [1], i.e.,

$$\left| \text{Re} \left( \frac{\lambda_t \Delta t}{\hbar} \right) \right| \leq 1. \quad (24)$$

In FFT language, the spatial eigenvalue problem Eq. (20) converts to

$$\lambda_s [\mathcal{A}^\dagger(\mathbf{r})\Psi] = \frac{\hbar^2}{2m} \mathcal{A}^\dagger(\mathbf{r}) \sum_{\ell=x,y,z} \mathcal{F}_\ell^{-1} [k_\ell^2 \mathcal{F}_\ell [\Psi]] + \gamma \mu_N \begin{pmatrix} B(\mathbf{r}) & 0 \\ 0 & -B(\mathbf{r}) \end{pmatrix} [\mathcal{A}^\dagger(\mathbf{r})\Psi], \quad (25)$$

where  $\mathcal{F}_\ell$  and  $\mathcal{F}_\ell^{-1}$  are the 1D FFT and its inverse along the  $\ell$  ( $\ell = x, y, z$ ) direction. Again we can apply the fact that the kinetic energy representable by a PSTD lattice has an upper limit. The maximum  $k$ s on the r.h.s. of Eq. (25) are  $\pm\pi/\Delta x$ ,  $\pm\pi/\Delta y$  and  $\pm\pi/\Delta z$  respectively. Any larger  $k$  will be aliased to a value within the limits. When we replace the  $k_x$ ,  $k_y$  and  $k_z$  with these maximum values, they can be extracted out from the inverse FFTs, resulting in  $\mathcal{F}_\ell^{-1} [\mathcal{F}_\ell [\Psi]] = \Psi$ , ( $\ell = x, y, z$ ). Therefore the kinetic energy term is bounded below

$$\frac{\hbar^2 \pi^2}{2m} \left( \frac{1}{\Delta x^2} + \frac{1}{\Delta y^2} + \frac{1}{\Delta z^2} \right) [\mathcal{A}^\dagger(\mathbf{r})\Psi]. \quad (26)$$

---

\*In case the magnetic field contains a KHz-MHz sweeping content, for a thermal neutron of 10meV, the cycle period of the de Broglie wave is at least 6 orders of magnitude smaller than the sweep cycle. The time variation of  $\mathcal{A}^\dagger$  is negligible within  $\Delta t$ . Thus, Eq. (23) still remains valid. The  $B$  in Eq. (28) takes the then-sweeping value, and  $\Delta t$  can also follow the  $B$  and be slowly swept over time.

We now notice the transformed wave function  $\mathcal{A}^\dagger(\mathbf{r})\Psi$  has a diagonalized upper bound form, and the upper bound for  $\lambda_s$  can be determined as

$$\lambda_s < \frac{\hbar^2 \pi^2}{2m} \left( \frac{1}{\Delta x^2} + \frac{1}{\Delta y^2} + \frac{1}{\Delta z^2} \right) + \gamma \mu_N B_{\max}. \quad (27)$$

Finally, combining Eqs. (24) and (27), the consistency requirement  $\lambda_t = \lambda_s$  leads to the sufficient (but not the necessary) stability condition of PSTD for the spinor wave function

$$\Delta t \leq \frac{\hbar}{\frac{\hbar^2 \pi^2}{2m} \left[ \frac{1}{\Delta x^2} + \frac{1}{\Delta y^2} + \frac{1}{\Delta z^2} \right] + \gamma \mu_N B_{\max}}. \quad (28)$$

The dimensionless version of Eq. (28) is

$$\Delta \tau \leq \left[ \pi^2 \left( \frac{1}{\Delta \bar{x}^2} + \frac{1}{\Delta \bar{y}^2} + \frac{1}{\Delta \bar{z}^2} \right) + \frac{\gamma \mu_N B_{\max}}{E_0} \right]^{-1}. \quad (29)$$

#### 4. Born approximation

Let the incident plane wave function be  $\Psi^{\text{inc}} = \begin{pmatrix} s_u \\ s_d \end{pmatrix} e^{i\mathbf{k}\cdot\mathbf{r}}$  with  $|s_u|^2 + |s_d|^2 = 1$ .

The Born approximation to Eq. (1) leads to the approximated solution of the spinor wave function

$$\Psi = \begin{pmatrix} s_u \\ s_d \end{pmatrix} e^{i\mathbf{k}\cdot\mathbf{r}} - \frac{\gamma m_n \mu_N}{2\pi \hbar^2} \frac{e^{ikr}}{r} \int d^3 r' e^{-i\mathbf{q}\cdot\mathbf{r}'} \begin{pmatrix} B_z(\mathbf{r}') & B_x(\mathbf{r}') - iB_y(\mathbf{r}') \\ B_x(\mathbf{r}') + iB_y(\mathbf{r}') & -B_z(\mathbf{r}') \end{pmatrix} \begin{pmatrix} s_u \\ s_d \end{pmatrix}, \quad (30)$$

with  $\mathbf{q} = \mathbf{k}' - \mathbf{k}$  the transferred wave vector and  $\mathbf{k}' = k\mathbf{r}/r$  the wave vector of the outgoing spherical wave.

#### 5. Modeling the neutron scattering by a uniformly magnetized sphere

A uniformly magnetized sphere is the simplest, realistic magnetic model. Its magnetic field carries a cylindrical symmetry around the internal magnetization. The magnetic induction  $B$  can be analytically derived and behaves as a magnetic dipole in the far field [25]. Furthermore, the volume integration in the scattering amplitude term on the r.h.s of Eq. (30) can be analytically carried out (Appendix A), avoiding the uncertainties coming from numerical integrations. A comparison between the PSTD predictions and the Born approximation can easily demonstrate the advantages of our method and quantify the limits of the latter.

Figure 1 employs a sphere of radius  $a$  with a uniform magnetization  $\mathbf{M}_0$  along the  $y$ -axis. The magnetic induction can be derived from the magnetic scalar potential [25], leading to

$$\mathbf{B}_\infty(\mathbf{r}) = \begin{cases} \frac{2}{3} \mu_0 M_0 \hat{y}, & \text{if } r < a \\ \mu_0 M_0 \frac{a^3}{r^3} \left[ \frac{xy}{r^2} \hat{x} + \left( \frac{y^2}{r^2} - \frac{1}{3} \right) \hat{y} + \frac{yz}{r^2} \hat{z} \right], & \text{if } r \geq a \end{cases} \quad (31)$$



An overall coefficient

$$V_0 = \gamma \mu_N \mu_0 M_0, \quad (32)$$

characterizes the energy-scale of the interacting potential and carries the dimension unit of energy. In the situation of monochromatic plane wave incidence, Eqs. (9) and (10) only depend on two ratios,  $V_0/E_0$  and  $a/\lambda_0$ . A scaling law of the differential scattering cross-section immediately follows, i.e.,

$$\frac{d\sigma}{d\Omega}(E_0, V_0, a) = \lambda_0^2 \frac{d\sigma}{d\Omega} \left( \frac{V_0}{E_0}, \frac{a}{\lambda_0} \right), \quad (33)$$

and consequently the absolute values of  $E_0$ ,  $V_0$ ,  $a$  no longer matter, and the only length scale  $\lambda_0$  is factorized out. The  $\frac{d\sigma}{d\Omega}$  on the r.h.s. of Eq. (33) depends on the two ratios and is dimensionless.

Outside the sphere,  $\mathbf{B}_\infty$  decays as  $r^{-3}$ . A cutoff of the interaction range is necessary for PSTD to proceed on a finite lattice. We set the  $r$ -cutoff to  $b = 8.175a$ , corresponding to 3-order of magnitude decay of interaction. To be exact, the actual magnetic induction under study is

$$\mathbf{B}_b(\mathbf{r}) = \mathbf{B}_\infty(\mathbf{r}) \Theta(r - b), \quad (34)$$

with  $\Theta(x)$  a step function, such that when  $x < 0$ ,  $\Theta(x) = 1$ , and  $x > 0$ ,  $\Theta(x) = 0$ .

Polarized magnetic neutron scattering exhibits anisotropic patterns. The scattering plane is best represented by its Euler angles. We use the  $y$ -convention for  $(\alpha, \beta, \gamma)$  [26]. The first two Euler angles for two characteristic planes are: the  $x - y$  plane,  $(\alpha, \beta) = (0^\circ, 0^\circ)$ ; and the  $y - z$  plane,  $(\alpha, \beta) = (0^\circ, 90^\circ)$ . The  $\gamma$  angle would easily label the direction of the outgoing wave on the plane.

To obtain the following results, we select a magnetic sphere of radius equal to one neutron wavelength, i.e.,  $a/\lambda_0 = 2\pi$ . The neutron plane wave is incident along the  $y$ -axis. An overlapping domain decomposition of  $1 \times 2 \times 1$  topology is mapped to a two-node parallel platform. A lattice of  $512 \times 320 \times 512$  grids is created on each subdomain, with  $\Delta\bar{x} = \Delta\bar{y} = \Delta\bar{z} = \pi/10$ , corresponding to 20 grids per wavelength. The time increment is  $\Delta\tau = \pi/1000$ , at the requirement of Eq. (29). The widths of the ABC, the SF, the transition layer, and the overlapping halo are 40, 41, 12 and 15 grids, respectively. The parameters for the ABC multiplier (Eq. (4)) are  $U_0 = 5.0$  and  $\alpha = 0.1/\text{grid}$ . The virtual surfaces are set right on the six middle planes of the SF.

To facilitate the comparison with the PSTD numerical results, we perform the volume integral on the r.h.s. of Eq. (30) upto the cutoff radius  $r' = b$  (Eq. (A.11)). A full Born approximation is straightforward by taken  $b \rightarrow \infty$ .

The simulations are conducted for two interaction strengths,  $V_0 = E_0/20$  and  $V_0 = E_0/2$ . Both the PSTD and the Born-approximation results are shown together on Figs. 2 and 3. On the left panels, the Euler  $\gamma$  angle sweeps from the  $+x$ -axis through the  $+y$ -axis and to the  $-x$ -axis, while on the right panels,  $\gamma$  sweeps from the  $-z$ -axis through the  $+y$ -axis and to the  $+z$ -axis. The interaction-strength dependent behaviors are not only manifested in the shape of the differential cross-sections, but also in the spin state to spin state transitions. For example, when the interaction is

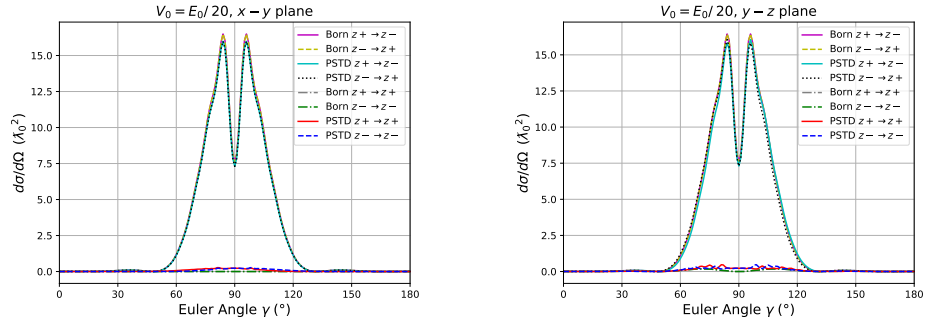


Figure 2: Differential cross-sections of the neutron scattering by extra weak magnetic field  $V_0 = E_0/20$ . The cutoff is at  $b = 8.175a$ .

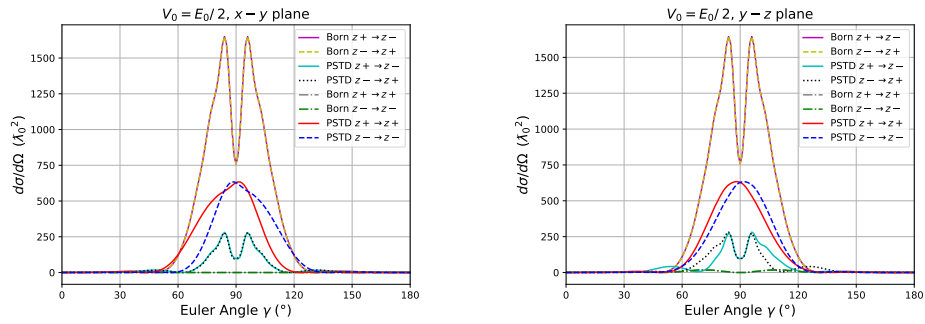


Figure 3: Differential cross-sections of the neutron scattering by weak magnetic field  $V_0 = E_0/2$ . The cutoff is at  $b = 8.175a$ .

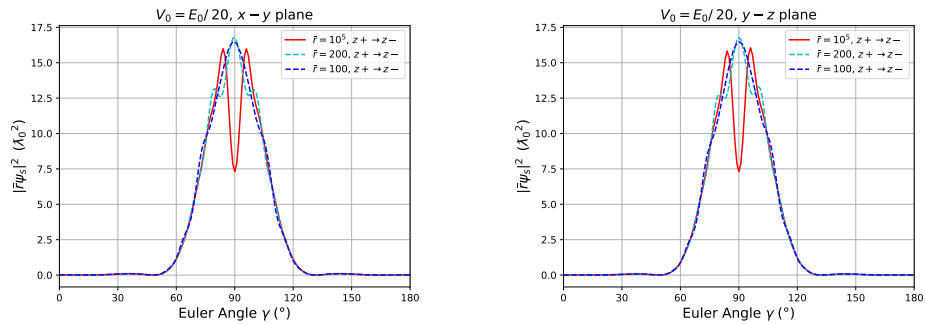


Figure 4: The PSTD solutions to the  $z^+ \rightarrow z^-$  scattering in the FR ( $\bar{r} = 100$  and  $\bar{r} = 200$ ) vs. in the far-field ( $\bar{r} = 10^5$ ). The magnetic interaction strength  $V_0 = E_0/20$ . The cutoff is at  $b = 8.175a$ .

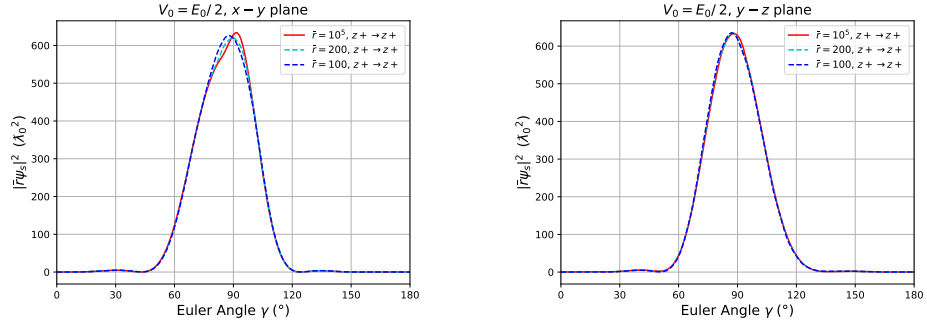


Figure 5: The PSTD solutions to the  $z^+ \rightarrow z^+$  scattering in the FR ( $\bar{r} = 100$  and  $\bar{r} = 200$ ) vs. in the far-field ( $\bar{r} = 10^5$ ). The magnetic interaction strength  $V_0 = E_0/2$ . The cutoff is at  $b = 8.175a$ .

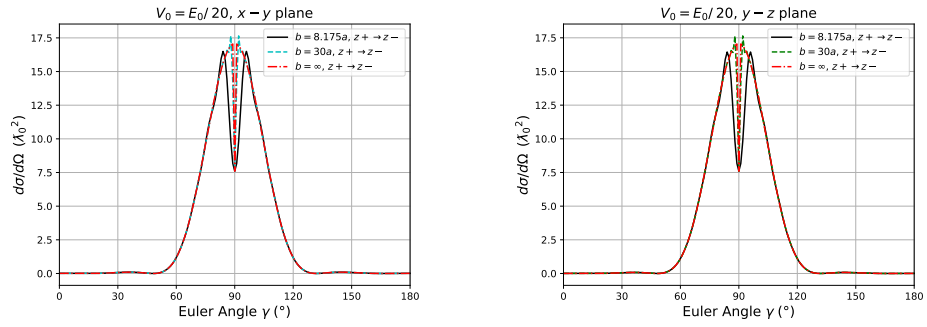


Figure 6: Effect of the interaction range cutoff on the results given by the Born approximation. The magnetic interaction strength  $V_0 = E_0/20$ .

weak  $V_0 = E_0/20$  (Fig. 2), the  $|z+\rangle \rightarrow |z-\rangle$  has higher probability than the  $|z+\rangle \rightarrow |z+\rangle$ , while it is the opposite when the interaction is 10 times as strong (Fig. 3).

In the Born-approximation, the interaction strength  $V_0$  enters as an overall factor in the scattered amplitude. When  $V_0$  goes from  $E_0/20$  to  $E_0/2$ , the shape of its differential cross-section remains the same, but the value becomes 100 times as large.

As expected, when the interaction is weak, the Born-approximation is very close to the exact result of PSTD (Fig. 2). However, when the potential becomes stronger (Fig. 3), the Born-approximation breaks down quickly. Thus, the PSTD solution can quantitatively assess the validity of the Born-approximation.

There exists an axial symmetry in this specific example we present. The magnetization  $\mathbf{M}_0$  is aligned on the  $y$ -axis and the incident wave is also along the  $y$ -direction. A rotation of the  $|z+\rangle$  spin state around the  $y$ -axis by  $180^\circ$  would give the  $|z-\rangle$  spin state, and vice versa. Thus Figs. 2-5 exhibit a flip-symmetry between the  $z+ \rightarrow z+$  and  $z- \rightarrow z-$  scatterings, as well as between the  $z+ \rightarrow z-$  and  $z- \rightarrow z+$  scatterings. Another feature in Fig. 3 is that the cross-sections show different shapes on the  $x-y$  plane and on the  $y-z$  plane.

Further numerical investigations using other incident spins reveal that the PSTD algorithm automatically obeys the supposition principle of quantum states, for example  $|x+\rangle = \frac{1}{\sqrt{2}}|z+\rangle + \frac{1}{\sqrt{2}}|z-\rangle$ . Therefore, the four scattering wave functions ( $z+ \rightarrow z+$ ,  $z+ \rightarrow z-$ ,  $z- \rightarrow z+$ , and  $z- \rightarrow z-$ ) form a complete set of the spin degree of freedom. The scattering wave function of arbitrary incident spin and outgoing spin can be expressed as a linear combination of the four basis.

Neutron ghost imaging detects the scattered neutrons in the FR. The magnetized sphere in this example is  $2\lambda_0$  in diameter. Its effective field spans  $20\lambda_0$ . A distance  $r \approx 400\lambda_0$  (i.e.,  $\bar{r} = 800\pi$ ) marks the transition from the FR to the far-field. In Figs. 4 and 5 we present the PSTD results at three distances,  $\bar{r} = 100$ ,  $\bar{r} = 200$ , and  $\bar{r} = 10^5$ . Big differences mainly exist in the forward angles, indicating the outgoing wave contains non-spherical wave content. This content evolves as the wave propagates.

*Effect from the cutoff of the interaction range* The magnetic induction  $\mathbf{B}$  of a magnetic dipole decays as  $r^{-3}$ . A numerical model, such as the PSTD we present, must constrain the lattice size. A cutoff on the interaction range is unavoidable. So far in this work, all the results are obtained under the cutoff  $b = 8.175a$ , with  $a$  the sphere radius. What will change if we push  $b$  beyond this limit? In Fig. 2, we see the results of the PSTD and the Born-approximation agree very well when the interaction is 5% the neutron energy. Under this limit, the Born-approximation can provide qualitative assessment of this cutoff. Using the analytical expression Eq. (A.11), the differential cross-sections are plotted for  $b = 8.175a$ ,  $b = 30a$  and  $b \rightarrow \infty$  (Fig. 6). We notice the differences are localized in the forward direction. In scattering experiments (as opposite to transmission ones), the forward angles are normally blocked by beam stop to absorb the unscattered incident neutrons. For  $b = 8.175a$ , this discrepancy occurs within  $\gamma \approx 90^\circ \pm 6^\circ$ . An increase of  $b$  narrows the angle span.

## 6. Summary

In this work, we incorporate the spin degree of freedom into the PSTD solver to the quantum potential scattering problems. Because the different spin compo-

nents are coupled through the off-diagonal elements of the interaction matrix, the PSTD algorithm for the scalar Schrödinger equation cannot be directly applied. The extension to the spinor version requires the simultaneous time-marching of both spin components satisfy a new stability condition. Once the virtual surface data of the up and down spin states are collected separately, the scalar version of the near-to-distant-field transform can be directly applied independently to each spin data. This lies on the fact that the magnetic field is absent outside the virtual enclosure, and thus the neutron spin will not precess while propagating out. The virtual surface data contain the complete information of the spinor wave function at any distant locations. Based on this development, magnetic neutron scattering can now be quantitatively investigated. In this paper, a uniformly magnetized sphere is used as an example to demonstrate the capability and accuracy of the algorithm. Much more complicated magnetic structure can be constructed and its neutron scattering straightforwardly calculated. This forms the forward model of the newly developed neutron ghost imaging (NGI) methodology [13]. By feeding the forward data to the NGI, the magnetization distribution can be reconstructed and compared with the original setup. Thus, the accuracy and efficacy of NGI can be evaluated. At last, our work supplies a numerical tool for other neutron magnetic analysis technologies as well.

### Acknowledgements

This work was supported by the National Natural Science Foundation of China under Grant Project No. 12075305.

### Appendix A. The volume integral involed in the Born-approximation

In the following detailed theoretical calculation on the Born approximation, it is the most convenient to adopt the conventional notation of the coordinate system (Fig. A.1), i.e., the direction of the magnetization  $\mathbf{M}_0$  is taken as the  $z$ -axis. For consistency, at the last step when Figs. 2 and 3 are plotted, the  $(\theta_q, \phi_q)$  angles in Fig. A.1 are translated into the Euler angles in Fig. 1. In addition, the spin states are also rotated using the D matrix.

With the arrangement in Fig. A.1, the magnetic induction becomes

$$\mathbf{B}_\infty(\mathbf{r}) = \begin{cases} \frac{2}{3}\mu_0 M_0 \hat{z}, & \text{if } r < a \\ \mu_0 M_0 \frac{a^3}{r^3} \left[ \frac{xz}{r^2} \hat{x} + \frac{yz}{r^2} \hat{y} + \left( \frac{z^2}{r^2} - \frac{1}{3} \right) \hat{z} \right], & \text{if } r \geq a \end{cases} \quad (\text{A.1})$$

The scattering amplitude from the Born approximation of Eq. (30) is essentially the linear combination of three volume integrals, i.e.,

$$\mathcal{I}_\ell = -\frac{\gamma \mu_N m_n}{2\pi \hbar^2} \int d^3r e^{-i\mathbf{q}\cdot\mathbf{r}} B_\ell(\mathbf{r}), \quad \ell = x, y, z. \quad (\text{A.2})$$

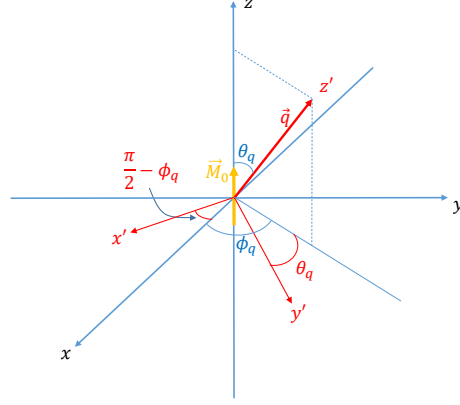


Figure A.1: The  $x - y - z$  and  $x' - y' - z'$  coordinate systems and the definition of the angles for the Born approximation calculation.

Because  $E_0 = \hbar^2/(2m_n\lambda_0^2)$ , the neutron mass  $m_n$  in Eq. (A.2) can be expressed in terms of neutron energy. Substituting Eq. (A.1) into Eq. (A.2) gives

$$\mathcal{I}_x = -\frac{V_0}{4\pi E_0 \lambda_0^2} \int_{a < r \leq b} d^3 r \frac{a^3 xz}{r^5} e^{-i\mathbf{q}\cdot\mathbf{r}}, \quad (\text{A.3})$$

$$\mathcal{I}_y = -\frac{V_0}{4\pi E_0 \lambda_0^2} \int_{a < r \leq b} d^3 r \frac{a^3 yz}{r^5} e^{-i\mathbf{q}\cdot\mathbf{r}}, \quad (\text{A.4})$$

$$\mathcal{I}_z = -\frac{V_0}{4\pi E_0 \lambda_0^2} \left[ \frac{2}{3} \int_{r \leq a} d^3 r e^{-i\mathbf{q}\cdot\mathbf{r}} + \int_{a < r \leq b} d^3 r \frac{a^3}{r^3} \left( \frac{z^2}{r^2} - \frac{1}{3} \right) e^{-i\mathbf{q}\cdot\mathbf{r}} \right]. \quad (\text{A.5})$$

Here, the parameters  $V_0$ ,  $a$  and  $b$  have been defined in the context. Due to the factor  $\exp(-i\mathbf{q}\cdot\mathbf{r})$ , it is not obvious how to proceed the integrations in the above equations. However, if we rotate the coordinate system so that  $\mathbf{q}$  lies on the  $z'$ -axis, we can take advantage of the cylindrical symmetry around the  $z'$ -axis to cancel odd symmetric terms.

Let  $\theta_q$  and  $\phi_q$  be the polar and azimuth angles of  $q$ , i.e.,

$$(\hat{q}_x, \hat{q}_y, \hat{q}_z) = (\sin\theta_q \cos\phi_q, \sin\theta_q \sin\phi_q, \cos\theta_q). \quad (\text{A.6})$$

As illustrated in Fig. A.1, a rotation around the  $z$ -axis clockwise by  $\frac{\pi}{2} - \phi_q$  would turn the  $x$ -axis to the  $x'$ -axis so that the latter is perpendicular to the  $\hat{z} - \hat{q}$  plane. The  $y$ -axis would now lie on the  $\hat{z} - \hat{q}$  plane. Then a rotation around the  $x'$ -axis clockwise by  $\theta_q$  would turn the  $z$ -axis to the  $\mathbf{q}$  direction. Consequently, a coordinate transformation follows

$$x = x' \sin\phi_q + y' \cos\theta_q \cos\phi_q + z' \sin\theta_q \cos\phi_q, \quad (\text{A.7})$$

$$y = -x' \cos\phi_q + y' \cos\theta_q \sin\phi_q + z' \sin\theta_q \sin\phi_q, \quad (\text{A.8})$$

$$z = -y' \sin\theta_q + z' \cos\theta_q. \quad (\text{A.9})$$

Substituting Eqs. (A.7)-(A.9) into Eq. (A.3), we have

$$\mathcal{I}_x = -\frac{V_0 a^3}{4\pi E_0 \lambda_0^2} \hat{q}_x \hat{q}_z \int_{a < r' \leq b} d^3 r' e^{i q z'} \frac{-y'^2 + z'^2}{r'^5}. \quad (\text{A.10})$$

In the above substitution and expansion of  $xz$ , we have dropped the cross-terms involving  $x'y'$ ,  $x'z'$ , and  $y'z'$  because they all integrate to 0 due to the cylindrical symmetry around the  $z'$ -axis. Derivations for  $\mathcal{I}_y$  and  $\mathcal{I}_z$  are similar. Further straightforward computations result in the scattered spherical wave

$$\Psi_{\text{Born}}^{\text{sca}} = \lambda_0 \frac{V_0}{E_0} \left( \frac{a}{\lambda_0} \right)^3 [F(qa) - F(qb)] \frac{e^{i kr}}{r} \left( \begin{array}{l} - \left[ \left( \hat{q}_x^2 + \hat{q}_y^2 \right) + \frac{2}{3} \frac{F(qb)}{F(qa) - F(qb)} \right] s_u + \hat{q}_z (\hat{q}_x - i \hat{q}_y) s_d \\ \hat{q}_z (\hat{q}_x + i \hat{q}_y) s_u + \left[ \left( \hat{q}_x^2 + \hat{q}_y^2 \right) + \frac{2}{3} \frac{F(qb)}{F(qa) - F(qb)} \right] s_d \end{array} \right), \quad (\text{A.11})$$

where

$$F(\rho) = \frac{\sin \rho}{\rho^3} - \frac{\cos \rho}{\rho^2}, \quad (\text{A.12})$$

and  $q = |\mathbf{q}|$ . We immediately notice the limits  $F(0) = 1/3$  and  $F(\infty) = 0$ . Because  $F(\infty) = 0$ , the limit of Eq. (A.11) at  $b \rightarrow \infty$  is obvious.

## References

- [1] K. Chen, A general PSTD method to solve quantum scattering in the Fresnel and far-field regions by a localized potential of arbitrary form, ArXiv e-prints (2024). [arXiv:2403.04053](https://arxiv.org/abs/2403.04053).
- [2] G. L. Squires, Introduction to the Theory of Thermal Neutron Scattering, Dover Publications, Mineola, New York, 1996.
- [3] Y. A. Izyumov, R. P. Ozerov, Magnetic Neutron Diffraction, Plenum Press, New York, 1970.
- [4] S. W. Lovesey, Theory of Neutron Scattering from Condensed Matter, Clarendon Press, Oxford, 1984.
- [5] Y. Zhu (Ed.), Modern Techniques for Characterizing Magnetic Materials, Kluwer Academic Publishers, Boston, 2005.
- [6] T. Chatterji (Ed.), Neutron Scattering from Magnetic Materials, Elsevier B.V., 2006.
- [7] H. Yu, R. Lu, S. Han, H. Xie, G. Du, T. Xiao, D. Zhu, Fourier-transform ghost imaging with hard X rays, Phys. Rev. Lett. 117 (2016) 113901.

- [8] D. Pelliccia, A. Rack, M. Scheel, V. Cantelli, D. M. Paganin, Experimental x-ray ghost imaging, *Phys. Rev. Lett.* 117 (2016) 113902.
- [9] S. Li, F. Cropp, K. Kabra, T. J. Lane, G. Wetzstein, P. Musumeci, D. Ratner, Electron ghost imaging, *Phys. Rev. Lett.* 121 (2018) 114801.
- [10] R. I. Khakimov, B. M. Henson, D. K. Shin, S. S. Hodgman, R. G. Dall, K. G. H. Baldwin, A. G. Truscott, Ghost imaging with atoms, *Nature* 540 (2016) 100.
- [11] A. M. Kingston, G. R. Myers, D. Pelliccia, F. Salvemini, J. J. Bevitt, U. Garbe, D. M. Paganin, Neutron ghost imaging, *Physical Review A* 101 (2020) 053844.
- [12] S. Gan, D. Z. Cao, K. Wang, Dark quantum imaging with fermions, *Phys. Rev. A* 80 (2009) 043809.
- [13] K. Chen, S. Han, Microscopy for atomic and magnetic structures based on thermal neutron Fourier-transform ghost imaging, *ArXiv e-prints* (2018). [arXiv: 1801.10046](https://arxiv.org/abs/1801.10046).
- [14] R. H. Brown, R. Q. Twiss, Correlation between photons in two coherent beams of light, *Nature* 177 (1956) 27.
- [15] R. H. Brown, R. Q. Twiss, A test of a new type of stella interferometer on sirius, *Nature* 178 (1956) 1046.
- [16] H. Klesel, A. Renz, F. Hasselbach, Observation of hanbury brown-twiss anticorrelations for free electrons, *Nature* 418 (2002) 392.
- [17] T. Rom, T. Best, D. van Oosten, U. Schneider, S. Folling, B. Paredes, I. Bloch, Free fermion antibunching in a degenerate atomic fermi gas released from an optical lattice, *Nature* 444 (2006) 733.
- [18] M. Iannuzzi, A. Orecchini, F. Sacchetti, P. Facchi, S. Pascazio, Direct experimental evidence of free-fermion antibunching, *Phys. Rev. Lett* 96 (2006) 080402.
- [19] M. Iannuzzi, R. Messi, D. Moricciani, A. Orecchini, F. Sacchetti, P. Facchi, S. Pascazio, Further evidence of antibunching of two coherent beams of fermions, *Phys. Rev. A* 84 (2011) 015601.
- [20] A. Taflove, S. C. Hagness, *Computational Electrodynamics, The Finite-Difference Time-Domain Method*, Third Edition, Artech House, Norwood, MA, 2005.
- [21] R. Kosloff, D. Kosloff, Absorbing boundaries for wave propagation problems, *J. Comput. Phys* 63 (1986) 363.
- [22] X. Gao, M. S. Mirotznik, D. W. Prather, A method for introducing soft sources in the PSTD algorithm, *IEEE Trans. Antennas Propaga.* 52 (2004) 1665.
- [23] A. A. Silaev, A. A. Romanov, N. V. Vvedenskii, Multi-hump potentials for efficient wave absorption in the numerical solution of the time-dependent Schrödinger equation, *J. Phys. B: At. Mol. Opt. Phys.* 51 (2018) 065005.



- [24] A. Soriano, E. A. Navarro, J. A. Porti, V. Such, Analysis of the finite difference time domain technique to solve the Schrödinger equation for quantum devices, *J. Appl. Phys.* 95 (2004) 8011.
- [25] J. D. Jackson, *Classical Electrodynamics*, the Third Edition, John Wiley & Sons, Inc., Hoboken, NJ 07030, 1999.
- [26] J. J. Sakurai, J. Napolitano, *Modern Quantum Mechanics*, Second Edition, Pearson Education, Inc., San Francisco, CA, 2011.